GEOPHYSICS, VOL. 79, NO. 2 (MARCH-APRIL 2014); P. S35–S46, 15 FIGS.
10.1190/GEO2012-0526.1

Downloaded 05/08/14 to 138.67.128.110. Redistribution subject to SEG license or copyright; see Terms of Use at http://library.seg.org/

Linearized wave-equation migration velocity analysis by image warping

Francesco Perrone[1], Paul Sava[1], Clara Andreoletti[2], and Nicola Bienati[2]

ABSTRACT

Seismic imaging produces images of contrasts in physical parameters in the subsurface, e.g., velocity or impedance. To build such images, a background model describing the wave kinematics in the earth is necessary. In practice, the structural image and background velocity model are unknown and have to be estimated from the acquired data. Migration velocity analysis deals with estimation of the background model in the framework of seismic migration and relies on two main elements: data redundancy and invariance of the structures with respect to different seismic experiments. Because all the experiments probe the same model, the reflectors must be invariant in suitable domains (e.g., shots or reflection angle); the semblance principle is the tool used to measure the invariance of a set of multiple images. We measure the similarity of the structural features between pairs of single-shot migrated images obtained from adjacent experiments. By using the estimated warping vector field between two migrated images, we construct an image perturbation which describes the difference in reflectivity observed by two shots. We derive an expression for the image perturbation that drives a migration velocity analysis procedure based on a linearization of the wave-equation with respect to the model parameters. Synthetic 2D examples show promising results in retrieving errors in the velocity model. This methodology can be directly applied to 3D.

INTRODUCTION

Seismic imaging aims to construct an image of geologic structures in the subsurface from reflection data recorded at the surface of the earth. For constructing such an image, one needs a model for computing the Green's functions that describe the wave propagation from source and receiver positions to every point in the subsurface. If we assume a linear, acoustic, and constant-density model, the velocity is the only parameter that governs the wave propagation. The correct velocity model is unknown and must be estimated from the data to obtain an accurate image of the reflectors in the subsurface, especially for highly heterogeneous geologic configurations.

Estimating the velocity model from the recorded data is referred to as *velocity analysis*. The problem is intrinsically nonlinear (because the solution of the wave-equation is a nonlinear function of the model parameters) and it is usually formulated as an optimization problem in which the correct velocity model minimizes an objective function, that is a measure of the model error. Two different classes of methods for estimating the wave propagation velocity have been discussed in the literature: data-domain methods, which we refer to as *waveform inversion* (WI) (Tarantola, 1984; Woodward, 1992; Pratt, 1999) and image-domain methods, usually referred to as *migration velocity analysis* (MVA) (Yilmaz, 2001; Sava and Biondi, 2004; Shen and Symes, 2008; Symes, 2008). WI operates in the data domain and iteratively updates the model parameters until the energy of the residual between simulated and recorded data is minimized. The WI objective function is characterized by numerous local minima (Bunks et al., 1995) and a good initial guess of the velocity model is necessary to converge to the correct solution. Migration velocity analysis relies on the assumption that the reflectors in the subsurface must be imaged at the same locations by different experiments. When the correct velocity model is used, the similarity between the images constructed for different experiments must be maximum. The similarity of the migrated images (i.e., the semblance principle [Sattlegger, 1975; Al-Yahya, 1989; Symes, 2008]) constitutes the criterion for designing an objective function that measures the quality of the velocity model.

Evaluating the semblance of a set of images requires constructing common-image gathers (CIGs), i.e., new images indexed in spatial position and an extension parameter, e.g., incidence angle, space/time lags (Rickett and Sava, 2002; Sava and Fomel, 2006; Yang

Manuscript received by the Editor 17 December 2012; revised manuscript received 1 November 2013; published online 10 February 2014.
[1]Colorado School of Mines, Department of Geophysics, Golden, Colorado, USA. E-mail: fperrone@mines.edu; psava@mines.edu.
[2]Eni S.p.A. — E&P Div., AESI Dept., San Donato Milanese, Italy. E-mail: clara.andreoletti@eni.com; nicola.bienati@eni.com.
© 2014 Society of Exploration Geophysicists. All rights reserved.

Downloaded 05/08/14 to 138.67.128.110. Redistribution subject to SEG license or copyright; see Terms of Use at http://library.seg.org/

and Sava, 2010), or experiments (Soubaras and Gratacos, 2007; Xie and Yang, 2008). In this paper, we present a measure based on the differential semblance criterion (Symes and Carazzone, 1991) for evaluating the correctness of the velocity model in the framework of migration velocity analysis. Our method operates in the image domain and computes the displacement vector field between two images. The displacement vector field is defined by a warping transformation of one image into the other and is pointwise measured by local crosscorrelations of the two images. The displacement vector field measures the apparent movement of an image with respect to its neighbor and can be used to extract the relative perturbation in reflectivity observed as a function of the shot position.

CIGs constructed at fixed lateral positions are unable to capture the full multidimensional apparent movement of the image point as a function of the extension parameter (Xie and Yang, 2008), for example, vertical and horizontal subsurface offset gathers must be combined together to completely estimate the movement of the image point in the subsurface when the structures are not mildly dipping (Biondi and Symes, 2004). Our technique measures the full vectorial shift of the image point and restates the semblance principle in terms of the consistency between the structural information in the image and the apparent displacement of image points as a function of experiments.

In the following sections, we describe the semblance principle, review the wave-equation MVA (WEMVA) procedure, and then introduce our approach for measuring the consistency of the velocity model based on the apparent shift between two images from adjacent shots.

IMAGE SIMILARITY, WARPING, AND VELOCITY ERRORS

The semblance principle

In seismic migration, the velocity model is assumed to be known, but in reality it represents the main unknown and has to be estimated from the data. MVA measures the similarity of the different migrated images (which are obtained by exploiting the redundancy of the data) using the semblance principle (Sattlegger, 1975; Al-Yahya, 1989). The semblance principle relies on the invariance of the subsurface with respect to the seismic experiments: because the model that generates the data is unique and time-invariant, different experiments must image the same structures. The quality of the migration result is assessed by constructing an image cube that collects the images as a function of the spatial coordinates $\mathbf{x}$ and experiment $R(\mathbf{x}, e)$ or extension parameter $R(\mathbf{x}, \alpha)$. The variable e indexes the experiments and can represent the shot number or the ray parameter in plane-wave migration; the extension parameter α can represent the reflection angle or the subsurface offset. The current practice consists in analyzing fixed spatial locations and considers all the experiments (Figure 1a) or all the values of the extension parameter (Figure 1b). If the velocity model is correct, the images show invariance along these dimensions in the image cube. This property is true in a kinematic sense: the reflection coefficients (Aki and Richards, 2002), which depend nonlinearly on the incidence angle, are neglected by this methodology. Several choices of domain are available for analyzing the invariance in the image cube; for example, the extended image domain (Rickett and Sava, 2002; Symes, 2008; Vasconcelos et al., 2010), the reflection angle domain (Biondi and Symes, 2004; Sava and Fomel, 2006), and the experiment domain (Chavent and Jacewitz, 1995; Mulder and Kroode, 2002; Soubaras and Gratacos, 2007; Xie and Yang, 2008).

The semblance principle can be implemented in different fashions:

1) In conventional semblance (Taner and Koehler, 1969), the energy of the stack of the migrated images measures the quality of the velocity model; the correct velocity model maximizes that energy.
2) In differential semblance (Symes and Carazzone, 1991), the energy of the first derivative along the extension axis measures the correctness of the velocity model; the correct model minimizes the energy.

Conventional and differential semblance are customarily implemented using gathers, e.g., common-reflection angle, to analyze the consistency between different results. Inconsistency in the migrated images appears as moveout in the gathers; the moveout is used for estimating the velocity error and for computing the velocity update

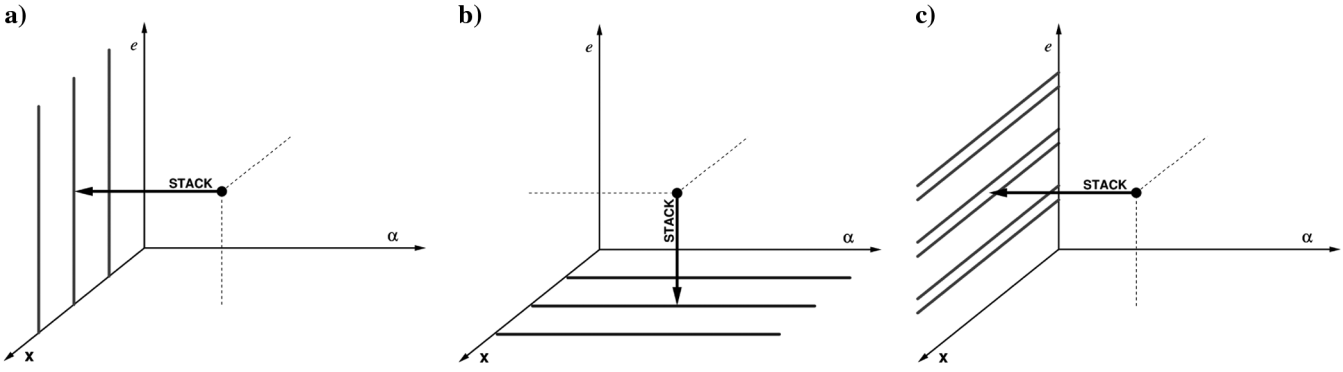


Figure 1. Migrated images can, in principle, be ordered in a hypercube and indexed by spatial location $\mathbf{x}$, experiment number e, and extension parameter α. By stacking along one of the axes, we reduce the dimensionality of the data and are able to analyze them. For example, we can stack along the extension parameter axis (e.g., reflection angle) and evaluate model accuracy by measuring the semblance at discrete positions in space between images corresponding to all experiment indices (a). Alternatively, by slicing together images from all experiments, we obtain CIGs (e.g., angle-domain CIGs), which we usually analyze at fixed spatial locations (b). A third option is to stack over the extension parameter and to analyze all points in the image for two (or a small number of) images obtained from nearby experiments (c). This last solution is what we propose in this paper.

Downloaded 05/08/14 to 138.67.128.110. Redistribution subject to SEG license or copyright; see Terms of Use at http://library.seg.org/

for the current model. If we consider CIGs, we have the situation depicted in Figure 1a and 1b. Because differential semblance considers similarities between adjacent experiments, in principle we can work without gathers in an iterative fashion by considering pairs of experiments (Figure 1c). This approach allows us to analyze all the points in the aperture of the two experiments at the same time, instead of constraining the appraisal of the velocity model at specific spatial locations where the CIGs have been constructed.

Image difference, image warping, and image perturbation

In this work, we explore a method for measuring similarity in the experiment domain. The experiment index may represent the shot number or the plane-wave ray parameter, and we consider all points in the aperture shared by adjacent shot-gathers. By "adjacent", we mean shot-gathers that illuminate the same portion of the subsurface and whose images show the same structures. The semblance principle is implemented in a differential sense by measuring the constructive interference of two images.

The easiest way to measure similarity between two migrated images R_i and R_j is to compute the difference

$$\Delta R(\mathbf{x}) = R_j(\mathbf{x}) - R_i(\mathbf{x}), \tag{1}$$

where the subscripts i and j denote the shot index and $\mathbf{x} = (x, y, z)$ is the position vector in the image domain. The signal ΔR represents the perturbation in the imaged reflectivity observed because of the change in shot position. If the velocity model is accurate, ΔR must be minimum because of the invariance of the reflector positions with respect to the shot location.

Image difference is a straightforward measure of similarity but, analogously to difference in the data domain, it is prone to cycle skipping. If the model is inaccurate, the difference in the position of the imaged reflectors can exceed half a cycle of the dominant wavelength and produce cycle skipping in the image domain. We address this problem using image warping (Hale, 2009). Image warping estimates a vector field $\mathbf{u}(\mathbf{x})$ that describes the apparent shift between two images by assuming the following relationship between the signals:

$$R_j(\mathbf{x}) = R_i(\mathbf{x} + \mathbf{u}(\mathbf{x})). \tag{2}$$

Correlation is a common tool to estimate shifts between two input signals. Some examples of their applications in the context of seismic imaging and velocity estimation are the work by Luo and Schuster (1991) and van Leeuwen and Mulder (2010). Local shifts can be estimated by extracting the correlation lag that maximizes the local correlations, i.e., correlations of the input signals in small local windows. In the image domain, the individual local correlations have the same dimensionality of the image and are as many as the points in the image. The efficient and fast computation of the local correlations can be performed using the procedure developed by (Hale, 2006). The estimation of the displacement field is more complex because it requires the extraction of the lag that maximizes the correlations. Searching the maximum of 2D (or 3D) local correlations becomes computationally expensive and less stable as the dimensionality increases. This problems can be addressed using a series of 1D shift estimations and warping along the coordinate axis (Hale, 2009). Hale et al. (2008) show an application of this method for estimating subsample shifts in time-migrated images for time-lapse monitoring.

If we assume that the warping field $\mathbf{u}(\mathbf{x})$ is small, we can rewrite equation 2 using a Taylor series expansion as

$$R_j(\mathbf{x}) \approx R_i(\mathbf{x}) + \nabla R_i(\mathbf{x}) \cdot \mathbf{u}(\mathbf{x}), \tag{3}$$

where $\nabla = ((\partial/\partial x), (\partial/\partial y), (\partial/\partial z))^T$ represents the gradient operator. Equation 3 allows us to rewrite equation 1 as

$$\Delta R(\mathbf{x}) \approx \nabla R_i(\mathbf{x}, s) \cdot \mathbf{u}(\mathbf{x}). \tag{4}$$

Vector displacements in the image domain are the analog of traveltime shifts in the data domain (Luo and Schuster, 1991; van Leeuwen and Mulder, 2010). The estimated shifts computed from a pair of images encode the information about their (phase) difference. The image perturbation, however, contains a single wavelet — that is, the wavelet of the reference image used in the estimation of the shifts. Exactly as traveltime shifts remove the cycle skipping problem in data differences, so the warping vector field does in the image domain. Of course, the correct estimation of the warping field is crucial for obtaining a reliable image perturbation.

The image gradient $\nabla R_i(\mathbf{x})$ is a vector that points in the direction of maximum increase in the image, and thus it is normal to the imaged reflector. By inspection, we observe that equation 4 is zero when the displacement vector field and the image gradient are orthogonal or, in terms of accuracy of the velocity model, the structural features (imaged reflectors) in migrated images obtained from adjacent experiments constructively interfere along the slope of the imaged reflector. Figure 2 shows the orientation of the dip and warping vector field for a horizontal interface and different perturbations of the velocity model. The dip field can be estimated using, for example, plane-wave destruction filters (Fomel, 2002) or gradient square tensors (van Vliet and Verbeek, 1995) whereas the warping field is computed by maximizing spatial local crosscorrelation of the input images at every spatial location (Hale, 2009). For this example, we measure the dip field by means of gradient square tensors, which estimate the orientation of features in multidimensional images by calculating the eigenvalues of the tensor obtained from the outer product of the gradient of the image at every point (van Vliet and Verbeek, 1995). Figure 2 shows the dip (solid arrows) and displacement vector field (dashed arrows) computed from the migrated images of a horizontal reflector; the velocity error is constant across the model. Note that only when the velocity model is correct are the two vector fields orthogonal at every image point. To obtain the image and the vector fields, we migrated two shots located at $x = 2$ km and $x = 2.05$ km, the horizontal interface is due to a density contrast and the velocity model is constant. The same reasoning applies to 3D images, where at every image point the image gradient is normal to the tangent plane of the reflector.

To design an inversion procedure, we need to link the image perturbations in equation 1 and 4 to an associated perturbation in the model. We use linearized WEMVA (Biondi and Sava, 1999; Sava and Biondi, 2004) to establish this link. Because of its simplicity, the image difference in equation 1 is suitable to derive the expression of the WEMVA operator for inversion. However, image difference is vulnerable to cycle skipping. The image-warping

Downloaded 05/08/14 to 138.67.128.110. Redistribution subject to SEG license or copyright; see Terms of Use at http://library.seg.org/

approximation in equation 4 of the image difference perturbation represents a more robust alternative for inversion.

WEMVA

We briefly review the theory of the linearized WEMVA approach (Biondi and Sava, 1999; Sava and Biondi, 2004) and then derive the linear operator that links the perturbation in the model Δs to the image perturbation ΔR that we defined in the previous sections. A detailed presentation of the WEMVA procedure can be found in Sava and Biondi (2004); implementation aspects are described by Sava and Vlad (2008).

Let us consider a reference model s and the associated wavefield $W(s,\omega)$, where ω represents temporal frequency. In the following, we drop the dependence on ω and s for the sake of readability. By

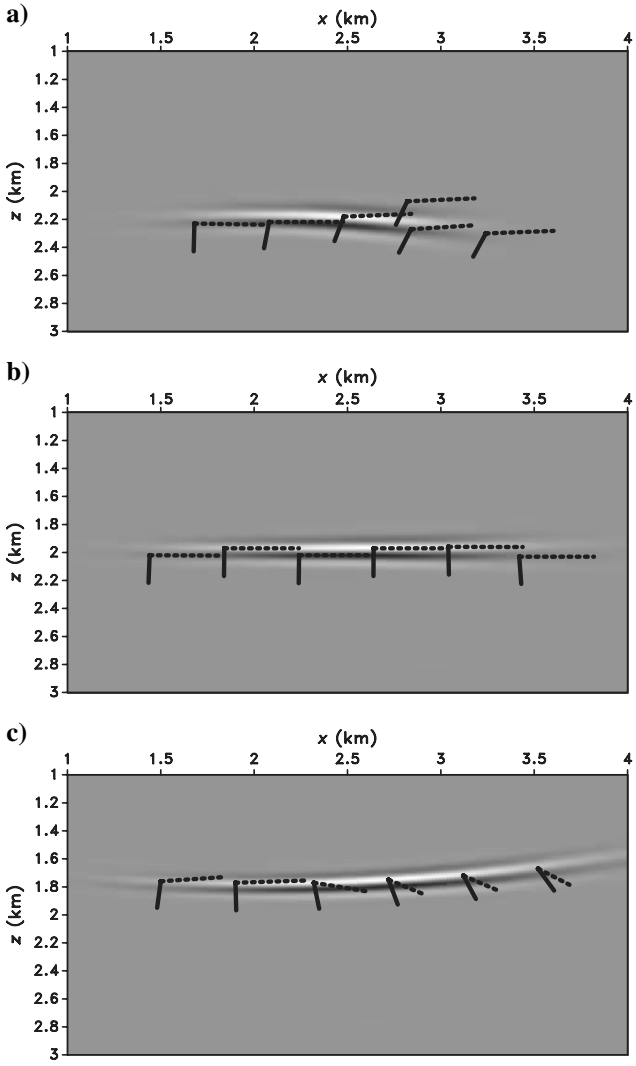


Figure 2. Horizontal density interface imaged using a single shot at $x = 2$ km and 800 receivers spaced 10 m at every grid point at the surface. The angle between the dip (solid arrows) and displacement vector field (dashed arrow) indicates a velocity error: (a) velocity too low, (b) correct velocity, and (c) velocity too high. The displacement vector field is computed using a second image obtained from a shot located at $x = 2.05$ km.

introducing a perturbation Δs in the model, we perturb W with a scattered wavefield δW. The mathematical expression for the scattered wavefield δW can be obtained once we define the form of the extrapolation operator $\mathbf{E}$ and scattering operator $\mathbf{S}$. Under the assumption that the perturbation is "small," we can use the linear Born scattering assumption to link the background and scattered wavefield. Following Sava and Biondi (2004), we denote by $\mathbf{E}$ the one-way downward continuation extrapolation operator and by $\mathbf{S}$ the associated Born scattering operator. We can then express the wavefield perturbation in terms of a linear operator applied to the model perturbation

$$\delta W = \mathbf{G}\Delta s, \tag{5}$$

where $\mathbf{G} = (\mathbf{1} - \mathbf{E})^{-1}\mathbf{ES}$ and $\mathbf{1}$ represents the identity operator (Sava and Biondi, 2004).

The image R depends on the slowness model s through the source and receiver wavefields W_S and W_R,

$$R = \sum_{\omega} \bar{W}_S W_R, \tag{6}$$

where the overline indicates the complex conjugate operator. The image R is linear in wavefields W_S and W_R; the imaging operator multiplies the two wavefields and stacks over the frequency axis. Despite the linearity of the image with respect to the wavefields, the image R depends nonlinearly on the model s; the nonlinearity comes from the nonlinear dependence on the parameters of the wave equation, which we have to solve to compute the source and receiver wavefields W_S and W_R. To linearize the relationship between the image and model, we assume a small perturbation Δs that would produce small perturbations in the wavefields. Equation 5 represents the mathematical expression of the linearized wavefield perturbations. By perturbing equation 6 with respect to source and receiver wavefields and neglecting second-order terms, we obtain

$$R + \delta R \approx \sum_{\omega} \bar{W}_S W_R + \sum_{\omega} \overline{\delta W}_S W_R + \sum_{\omega} \bar{W}_S \delta W_R, \tag{7}$$

where δW_S and δW_R are the linear perturbations in the source and receiver wavefields resulting from a perturbation Δs in the slowness model. Here, δR represents the perturbation that would be observed in the image. Using equation 7, we can relate the image perturbation δR and the wavefield perturbation by removing the background image from the left and right side of the equation to obtain

$$\delta R \approx \sum_{\omega} \overline{\delta W}_S W_R + \bar{W}_S \delta W_R. \tag{8}$$

By using equation 5, we can link the image perturbation δR to the model perturbation Δs through a cascade of linear operators,

$$\delta R = \left(\sum_{\omega} W_R \bar{\mathbf{G}}_S + \bar{W}_S \mathbf{G}_R \right) \Delta s, \tag{9}$$

where $\mathbf{G}_{S,R}$ represents the extrapolation/Born scattering operator for the source (S) or receivers (R) side.

We estimate the image perturbation ΔR for our inversion scheme starting from the difference of adjacent shots. Let us consider two images $R_i = R_i^c + \delta R_i$ and $R_j = R_j^c + \delta R_j$. Each of them is the

Downloaded 05/08/14 to 138.67.128.110. Redistribution subject to SEG license or copyright; see Terms of Use at http://library.seg.org/

superposition of the image in the background correct model (R_i^c and R_j^c) and the image perturbation caused by the model perturbation Δs (δR_i and δR_j); then the difference of the two images is

$$\Delta R = R_j(\mathbf{x}) - R_i(\mathbf{x}) = R_j^c(\mathbf{x}) - R_i^c(\mathbf{x}) + \delta R_j - \delta R_i. \quad (10)$$

For shots that illuminate the same portion of the subsurface, the difference between the images obtained using the correct model is negligible compared to perturbation terms, and equation 10 reduces to

$$\Delta R \approx \delta R_j - \delta R_i. \quad (11)$$

Equation 11 shows that, under the assumption of small separation between the shots, the image sdifference $R_j(\mathbf{x}) - R_i(\mathbf{x})$ gives us an approximation of the image perturbation we need for the WEMVA operator. Finally, by combining equations 9 and 11, we can link the image perturbation ΔR to the model perturbation Δs through a linear operator

$$\Delta R = \mathbf{L}\Delta s, \quad (12)$$

where

$$\mathbf{L} = \left(\sum_{\omega} W_{R,j}\bar{\mathbf{G}}_{S,j} - W_{R,i}\bar{\mathbf{G}}_{S,i} + \bar{W}_{S,j}\mathbf{G}_{R,j} - \bar{W}_{S,i}\mathbf{G}_{R,i}\right) \quad (13)$$

relates the perturbation in the model parameters Δs to the image perturbation ΔR through the cascade of the scattering operator $\mathbf{G}_{S,R}$ and the wavefields computed in the current model $W_{S,R}$. We use the operator derived from the image difference to invert the image perturbation estimated with image warping.

Workflow

We implement a nonlinear inversion scheme based on the solution of a sequence of linearized problems. Each linearized problem is solved using a standard conjugate gradient algorithm. Given an initial velocity model, we compute the associated migrated images for a pair of adjacent shot-gathers. From the migrated images, we compute the displacement vector field that warps one image into the image obtained from the adjacent shot using the efficient algorithm described in Hale (2009). The vector shifts are computed using local correlations as a series of 1D shifts along the coordinate axis of the input images. We also compute the smooth image gradient for each migrated image. The smooth gradient is the cascade of the ∇ operator and a low pass Gaussian filter to avoid the amplification of high-frequency random noise. The dot product between the image gradient and the displacement field associated with the relative shot gives the image perturbation that drives the linearized MVA algorithm. The linearized MVA procedure (Sava and Biondi, 2004) links the perturbation in the slowness model to the image perturbation via a linear operator. The goal is to solve the system

$$\mathbf{L}\Delta s = \Delta R, \quad (14)$$

where the operator $\mathbf{L}$ and the image perturbation ΔR are defined in the previous sections. We solve the linear problem using the conjugate gradient method. The solution of linear problem is an estimate of the model perturbation. This perturbation is added to the current model and we iterate the steps above until the stopping criterion is satisfied. The intermediate model update modifies the operator $\mathbf{L}$ and thus allows us to solve the nonlinear problem through a series of linearized approximations. For each linearized step, we perform five conjugate gradient iterations. The number of iterations of conjugate gradient for each linearized step has been chosen heuristically by looking at a single iterations and the change of the estimated model perturbation. We observed no major changes after five iterations. The nonlinear inversion is performed by iterating until a certain criterion is met: either the energy of the image perturbation ΔR falls below a certain threshold or a maximum number of iterations is reached; in this paper, we fix the maximum number of iterations.

NUMERICAL EXAMPLES

Equation 3 shows that image warping is an approximation of the image difference if we assume that the warping vector field $\mathbf{u}$ is able to track the apparent displacement between the two images. Nonetheless, the image perturbation obtained from image warping depends on only one image and is thus intrinsically more robust against cycle-skipping. We show a comparison between the sensitivity kernels obtained by backprojecting the image perturbation obtained from the forward WEMVA operator, from image warping, and from image difference, and demonstrate the superiority of image warping. We apply our methodology to two inversion tests. In the first one, we consider a simple model with a stack of horizontal density interfaces in a vertical velocity gradient; the correct model is perturbed by two Gaussian anomalies with opposite sign. We conclude the section showing the inversion results obtained on the Marmousi data set using a limited number of shot gathers. Our methodology is able to correct the model and obtain a more geologically plausible image.

Sensitivity to cycle-skipping and backprojections

Let us consider the model in Figure 3. The reflecting interface in Figure 3a is due to a density contrast. We model the data with a two-way finite-difference algorithm in the vertical gradient of slowness in Figure 3b. We migrate the data with a downward continuation operator (Stoffa et al., 1990) and different amplitudes of the velocity anomaly in Figure 3c. We migrate two shots located at $x = 2$ km and $x = 2.05$ km for each perturbation, compute the image perturbations using image difference and image warping, and compute the backprojections using the adjoint of the WEMVA operator. The columns of Figure 4 show backprojection for different signs of the Gaussian anomaly; the left column is the case of a fast anomaly, whereas the right column is the case of a slow anomaly. The peak value of the anomaly is ± 0.5 km/s. The rows of Figure 4, from top to bottom, show the backprojection in the ideal case, where the image perturbation is obtained from the forward WEMVA operator, the backprojection obtained using the image perturbation computed using image warping, and finally the backprojection obtained using the image difference. Observe that image warping leads to smoother backprojections that better approximate the ideal results. The highly oscillatory behavior of the backprojections obtained from image difference is due to cycle skipping in the image domain. The warping vector field encodes the shift between the two images, the image

Downloaded 05/08/14 to 138.67.128.110. Redistribution subject to SEG license or copyright; see Terms of Use at http://library.seg.org/

perturbation obtained by image warping depends on a single image and is thus immune from cycle-skipping problems as long as the warping vector field is accurately estimated.

The backprojections of the estimated image perturbations contain sidelobes, which have been observed in other migration velocity analysis algorithms (Fei and Williamson, 2010); we conjecture that these artifacts are attributable to the actual nonlinearity of the estimated image perturbation with respect to the model parameters.

Inversion test

As mentioned before, the estimation of model parameters for wave phenomena is a nonlinear problem because the solution of the wave equation is nonlinear in the model parameters (slowness, density, etc.). To test our inversion methodology, we use custom implementation of a nonlinear scheme based on the conjugate gradient algorithm (Vogel, 2002), in which the nonlinear problem is first linearized and an approximate solution is obtained. The approximate solution is then used to obtain a new linearization and then a new approximate solution, and so on. For every nonlinear iteration, we recompute the images and solve a linearized problem assuming the new background medium. The model for the inversion is shown in Figure 5: in Figure 5a, the reflectors arise from density contrasts and, in Figure 5b, the correct slowness model is a simple vertical gradient. We consider 24 pairs of shots at the surface; the receiver are evenly spaced by 20 m at each grid point at the surface. The shots in each pair are 50 m apart and the spacing between the pairs is 250 m; the shot pairs do not overlap.

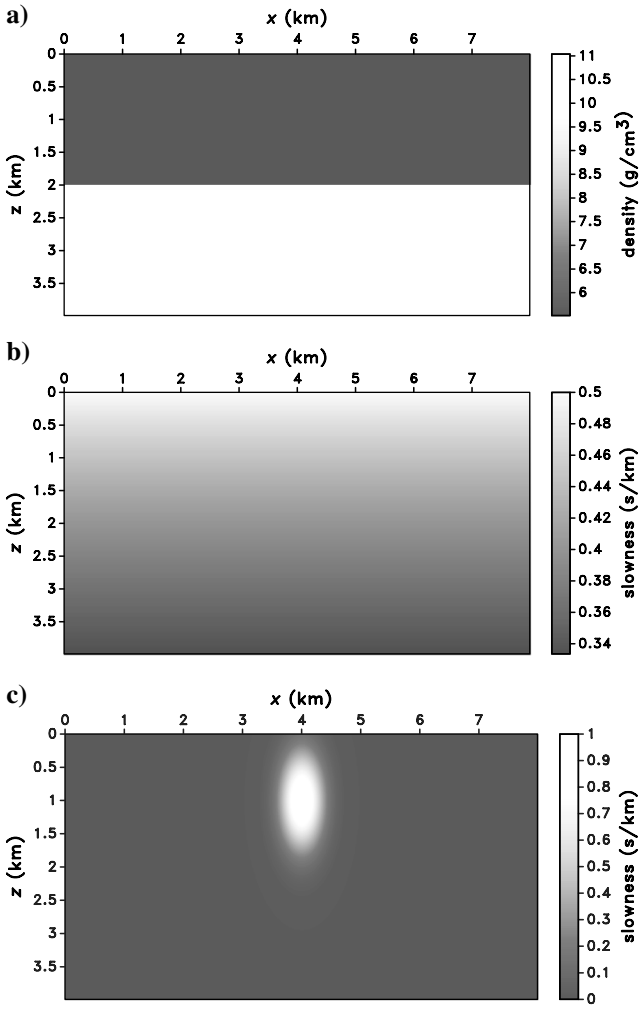


Figure 3. Vertical section of a 3D model with azimuthal symmetry. (a) Density model, (b) background slowness model, and (c) slowness anomaly.

The initial and updated velocity model are shown in Figure 6. The data for the inversion test are computed through full-acoustic time-domain finite-difference modeling and Gaussian random noise is added to each shot-gather separately. The signal-to-noise ratio is 10. Absorbing boundary conditions are implemented to avoid surface-related multiples; the internal multiples generated by the reflectors in the model are not subtracted from the data and constitute additional source of noise. In the examples, the absolute value of the peak of the velocity anomaly is 200 m/s, which is 10% of the minimum value of the background velocity gradient. Nonetheless, the shape of the velocity anomaly causes severe focusing/defocusing of the wavefield (depending on the sign of the anomaly), which makes migration velocity analysis challenging, especially in the initial steps.

We run a nonlinear inversion involving five conjugate-gradient iterations for each linearized step. We stop after 13 iterations, when the objective function starts oscillating, which indicates we reached a minimum of the objective function. Figure 6 shows that the initial Gaussian-shaped anomalies are smoothed out by the migration velocity analysis procedure. Figure 7 shows the resulting migrated images for the initial velocity model and that after 13 nonlinear iterations. Observe the improved focusing of the image, especially for the deepest reflectors. Figure 8 shows the comparison of the correct model (solid line) with the initial (dotted line) and inverted (dashed line) slowness model at $x = 2.5$ km and $x = 5.5$ km. The inversion partially corrects the anomaly but does not completely eliminate it. In Figure 8, we observe that the algorithm is more effective in the case of a positive slowness anomaly rather than a negative anomaly. We speculate that this behavior may be due to the fact that the image contains more energy at $x = 5.5$ km than at $x = 2.5$ km because of the opposite effects of the two anomalies on the imaged reflectors. Nonetheless, the correction applied to the slowness model is sufficient to flatten the image of the reflectors and remove the triplications from the image.

Figure 9 shows the decrease of the energy of the image perturbation with the number of iterations. After 13 iterations, the objective function increases, which means that we reached the minimum and the algorithm starts oscillating around the minimum. We stopped the inversion when the objective function stops decreasing after 14 iterations and show the result after 13 iterations. The nonzero value of the energy of the image perturbation results from several factors: the random noise in the data, internal multiples, and the size of the local window used to compute the dip and displacement field; all of them constrain the accuracy, resolution, and sensitivity we can achieve. No regularization is implemented; the footprint of the acquisition geometry is clearly visible in the inversion result, and it represents an additional source of noise.

Local Marmousi inversion

In this section, we consider a more complex synthetic example. Figure 10 shows the correct macro velocity model for the Marmousi data set and the anomaly used in the inversion test. The model in

Downloaded 05/08/14 to 138.67.128.110. Redistribution subject to SEG license or copyright; see Terms of Use at http://library.seg.org/

Figure 10a is obtained by smoothing the exact Marmousi with a 15-sample vertical and 30-sample horizontal triangular filter. We generate the data by single-scattering Born finite-difference modeling; the reflectivity profile is the vertical derivative of the exact Marmousi model. We want to show the ability of our method of recovering model perturbation using a limited number of experiments (shots in this case); we consider 12 shots, evenly spaced by 0.04 km at the surface; the first shot is positioned at $x = 0.96$ km. The receivers are spaced 0.008 km on the surface and they are located at every grid point.

The anomaly is Gaussian-shaped, with peak velocity 0.2 km/s and is subtracted from the correct velocity field. The perturbation in slowness is obtained by converting to slowness the correct and perturbed model and taking the difference of the former from the second. Notice the complicated shape that comes from the nonlinear relationship between velocity and slowness. The minimum amplitude of the perturbation is about −0.03 s/km, which is about 10% of the local background slowness but other areas are more strongly perturbed. Figure 11a shows the image of the 12 shot gathers considered in the correct model; by comparing the correct image with the image obtained using the initial model (Figure 11b) we observe that several structural features are distorted and the continuity of some reflectors broken (compare reflectors at lateral position $x = 2$ km). After 20 nonlinear iterations, we obtain the image in Figure 11c: The bottom reflector is now more continuous and the shape and amplitude of the dipping reflector in the middle section have been corrected. We also want to stress that these results do not involve any regularization or shaping of the estimated anomaly, which would greatly speed up convergence. Figure 12 shows the comparison of the exact perturbation used in the test with the inverted anomaly. Our linearized migration velocity analysis algorithm is able to recover the location of the anomaly and the

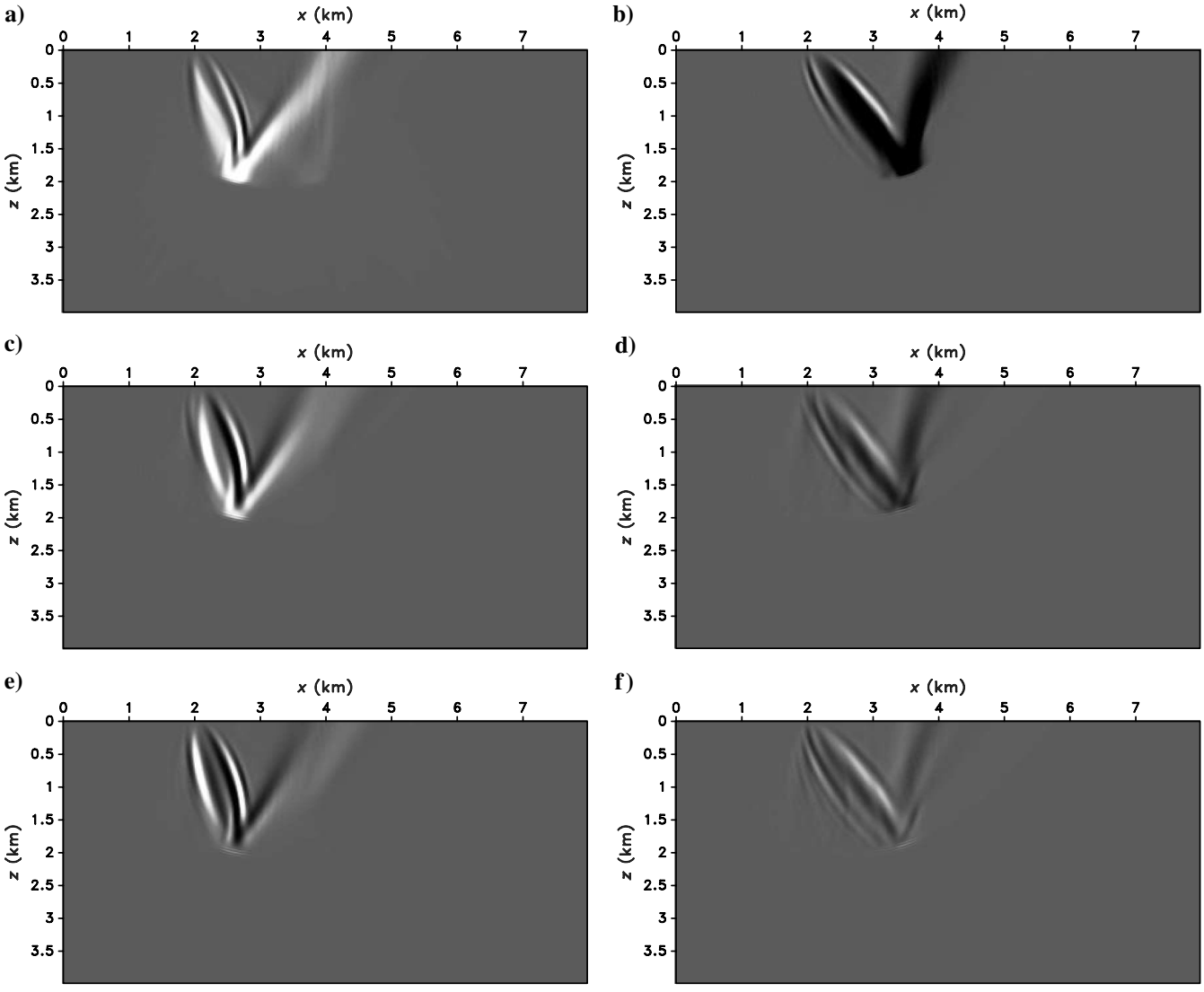


Figure 4. (a, c, and e) show the backprojection of image perturbations for a positive value of the anomaly in Figure 3c. The image perturbations are obtained by forward WEMVA operator, image warping, and image difference respectively. (b, d, and f) show the backprojections obtained for a negative anomaly. Image warping consistently produces smoother backprojections that better approximate the ideal cases in (a and b). The oscillations in the backprojections of image differences are connected with cycle-skipping problems.

Downloaded 05/08/14 to 138.67.128.110. Redistribution subject to SEG license or copyright; see Terms of Use at http://library.seg.org/

magnitude of the perturbation. Figure 13 shows the comparison of the initial (dotted line), inverted (dashed line), and correct (solid line) slowness model at $x = 2.5$ km, where the anomaly is the strongest. Observe that the inversion reduces the discrepancy between the initial and correct model. Figure 14 shows the evolution of the energy of the image perturbations with the number of iterations, which rapidly decreases to 10% of the initial value and then flattens. We want to emphasize that we are able to correct the anomaly in the model using a small number of shots despite the lack of full illumination whereas methods based on focusing measures (i.e., MVA based on extended images) need complete angular

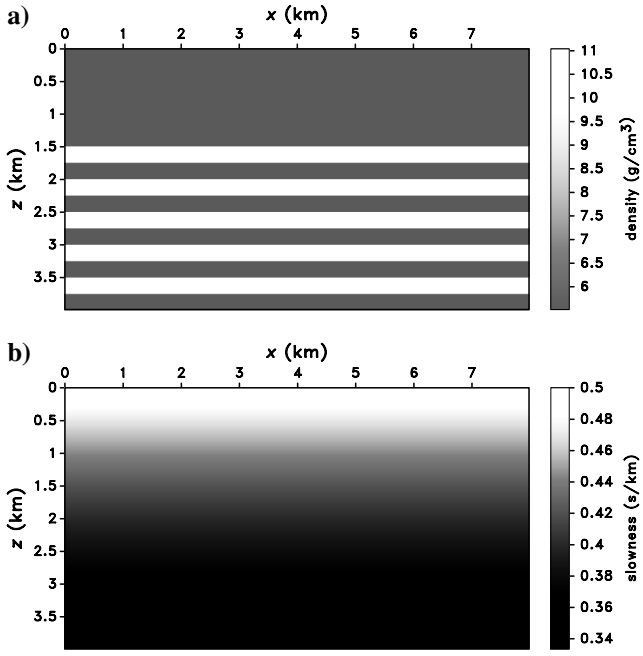


Figure 5. Model for the inversion test. (a) Stack of layers with alternating values of density; (b) Correct slowness model.

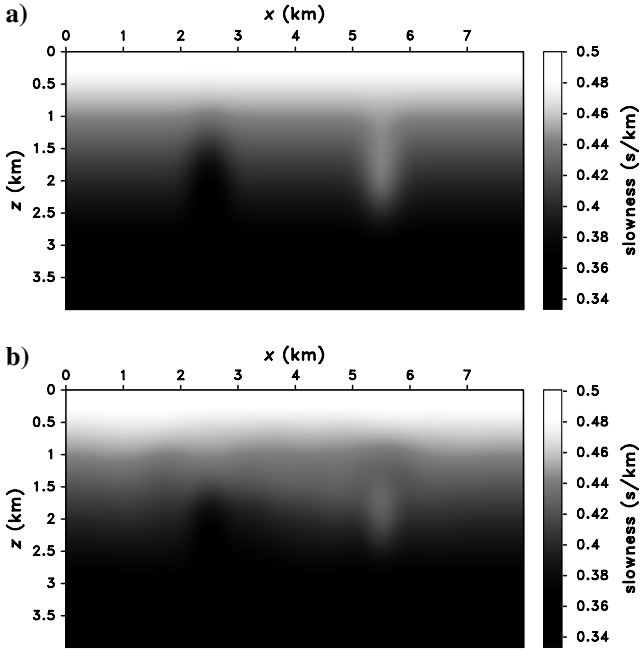


Figure 6. Slowness model: (a) initial and (b) inverted after 13 nonlinear iterations.

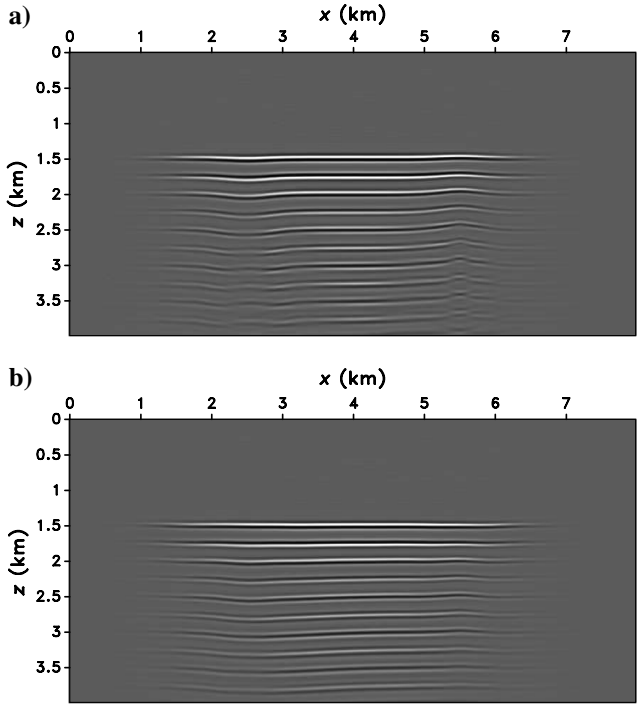


Figure 7. Migrated images: (a) image obtained with the initial velocity model and (b) after 13 velocity updates. The image in (b) is obtained after 13 nonlinear iterations; every linearized problem involves five iterations of conjugate gradient. Note the better focusing of the image.

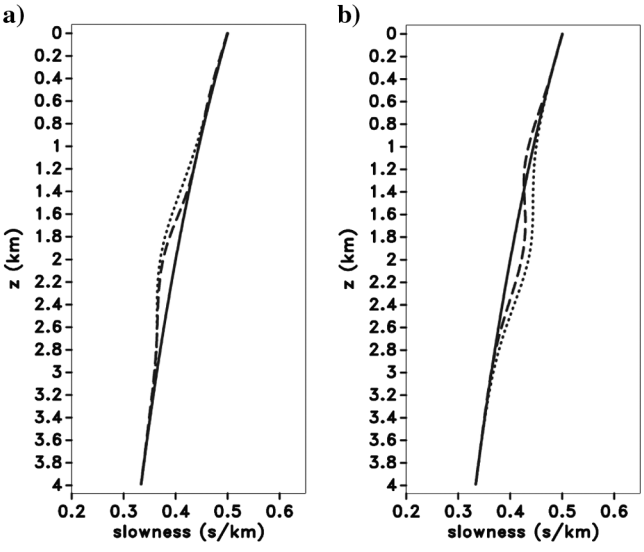


Figure 8. Comparison of the initial (dotted line), inverted (dashed line), and exact (solid line) slowness model at (a) $x = 2.5$ km and (b) $x = 5.5$ km. The inversion reduces the anomaly but does not eliminate it. Nonetheless, the reflectors in Figure 7b are flattened.

Downloaded 05/08/14 to 138.67.128.110. Redistribution subject to SEG license or copyright; see Terms of Use at http://library.seg.org/

coverage to evaluate focusing in the image domain. Figure 15 shows the shot-domain CIGs computed before and after inversion. The gathers show improved flatness and focusing after inversion despite the fact that we did not use explicitly the curvature of the CIGs to drive the inversion.

DISCUSSION

Our image perturbation approximates the image difference, but is by construction more robust against cycle skipping in the image domain. Our image warping approximation can also be interpreted as a measure of constructive interference of pairs of images

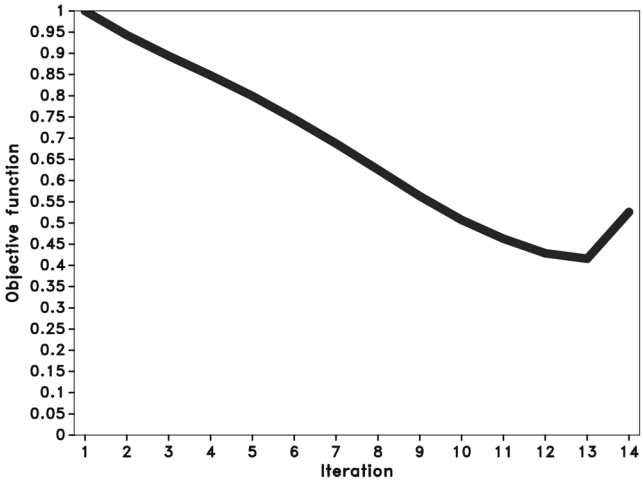


Figure 9. The decrease of the energy of the image perturbation indicates that we are approaching the correct model. We stopped the inversion after 13 iterations because the objective function starts oscillating, which indicates that we reached a minimum of the objective function.

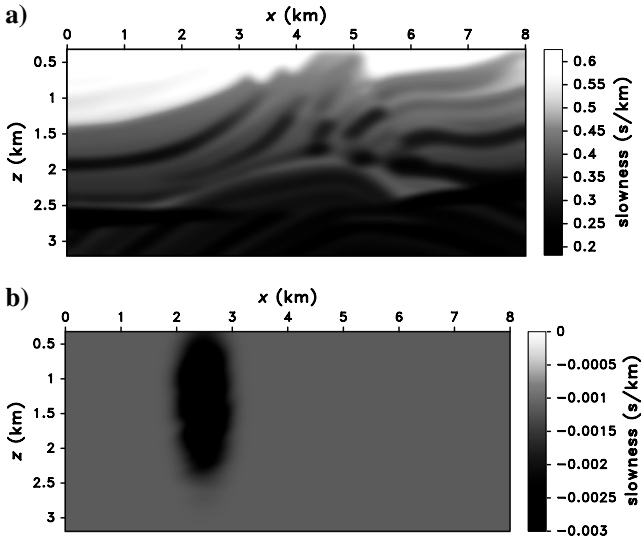


Figure 10. Macro slowness model (a) for the Marmousi data set and (b) slowness perturbation for the model in (a).

using the warping field that relates them and the structural dip. The velocity error produces shifts of the image points, which can be observed in the image cube as moveout as a function of an extension parameter (e.g., the reflection angle or the shot index). The moveout represents a velocity error indicator and is inverted for updating the velocity model. In the literature (Biondi and Symes, 2004; Sava and Fomel, 2006; Xie and Yang, 2008), the assumption of a shift along the normal to the reflector is commonly made; however, as Xie and Yang (2008) point out, this is just an approximation in a general case of complex geology and velocity model. Moreover, the residual moveout is often measured along just the vertical direction, i.e., in CIGs, rather than along the normal to the reflector, and then converted into the normal residual moveout using simple trigonometry. That approach relies on the assumption that the dip of the reflector is independent of the velocity in the overburden. In general, this is not true. Our approach directly evaluates the degree of constructive interference of adjacent experiments and does not rely on any assumption about the direction of the shift of the image point in the migrated domain. Moreover, we are able to measure the

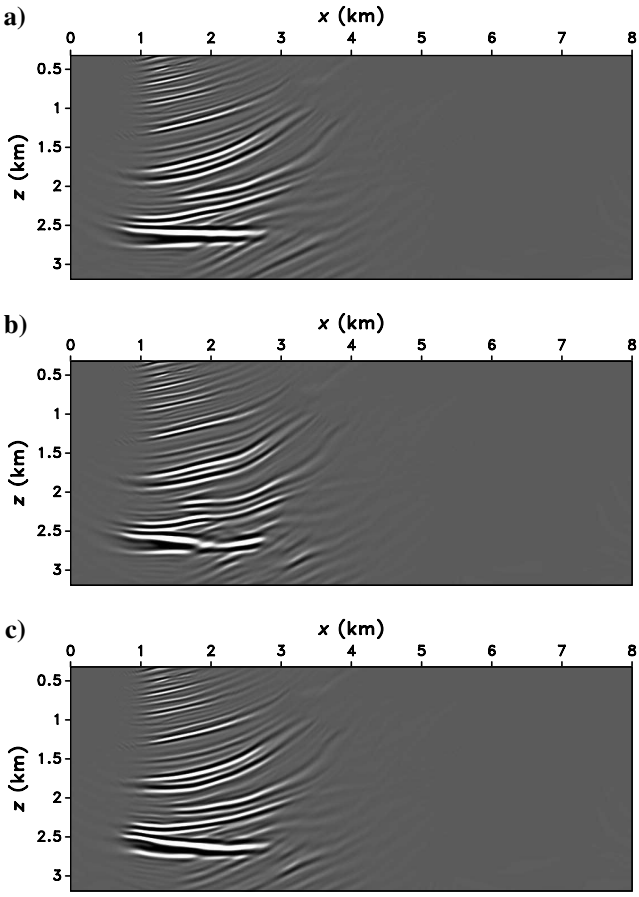


Figure 11. Image obtained using the correct slowness model (a), initial migrated image (b), migrated image after 20 nonlinear iterations (c). We consider 12 shots, evenly spaced by 0.04 km at the surface; the first shot is positioned at $x = 0.96$ km. The receivers are spaced 0.008 km on the surface and they are located at every grid point. Observe the improved continuity of the bottom reflector and the correction of the distortion of the middle dipping interfaces at a lateral position about $x = 2$ km.

Downloaded 05/08/14 to 138.67.128.110. Redistribution subject to SEG license or copyright; see Terms of Use at http://library.seg.org/

3D shift of the image point between the two experiments and then capture the complete kinematic information.

MVA is based on kinematic assumptions: the correct velocity model returns a prestack image cube characterized by *horizontal* events along the experiment axis. Note that we say *horizontal* and not *constant in amplitude*, highlighting the kinematic nature of the conventional semblance principle. As already discussed by Mulder and Kroode (2002), the amplitudes of images from nearby experiments are likely to be similar but not equal. Reflection coefficients should be taken into account, and the velocity model itself, if it is highly heterogeneous, can lead to important differences in the amplitudes.

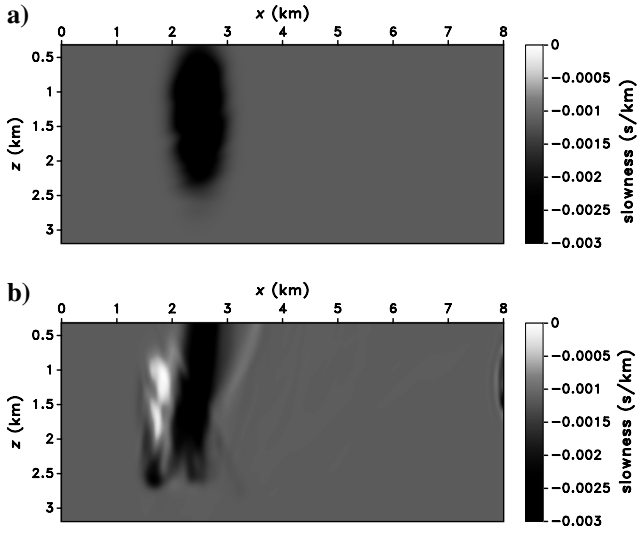


Figure 12. (a) Exact slowness perturbation and (b) inverted anomaly after 20 iterations of linearized migration velocity analysis. We correctly recover the location and magnitude of the perturbation.

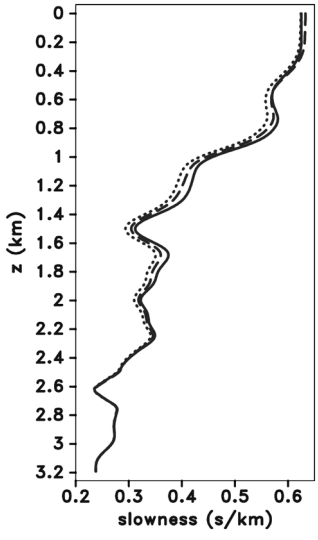


Figure 13. Comparison of the initial (dotted line), inverted (dashed line), and exact (solid line) slowness model at $x = 2.5$ km. Observe that inversion corrects the large discrepancy between the initial and correct model.

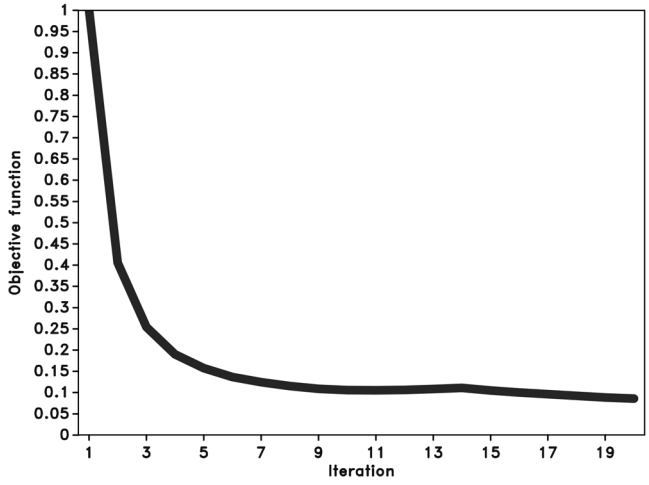


Figure 14. The energy of the image perturbation decreases rapidly and reaches convergence.

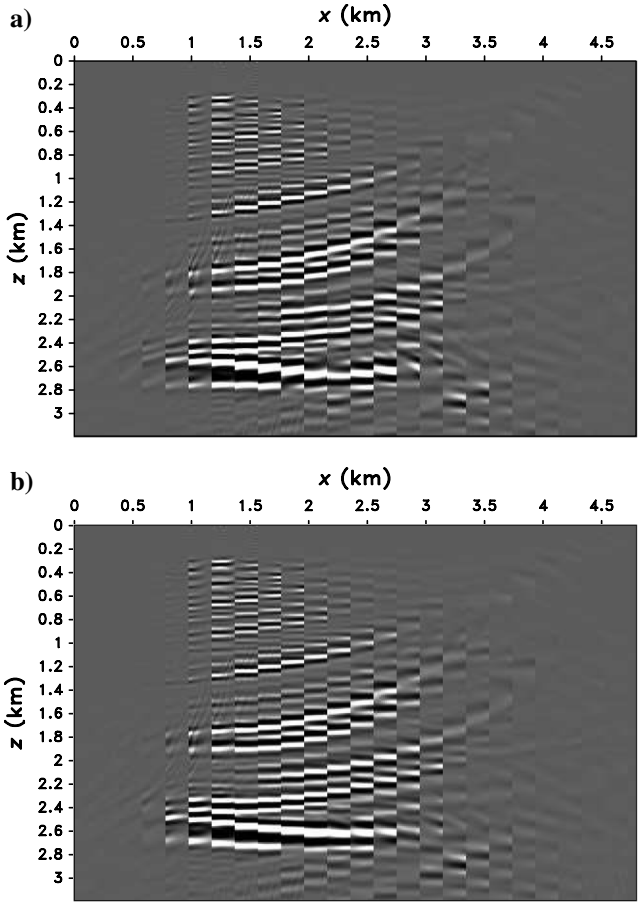


Figure 15. Shot-domain CIGs (a) before inversion and (b) after 20 iterations of linearized migration velocity analysis. Although the curvature of these CIGs is not explicitly used in the inversion, we are able to improve flatness and focusing.

Downloaded 05/08/14 to 138.67.128.110. Redistribution subject to SEG license or copyright; see Terms of Use at http://library.seg.org/

The measure of velocity error is independent of the migration algorithm and in principle either a one-way or a two-way velocity update engine can be used. The current implementation of the our WEMVA procedure relies on a one-way operator; the extension to two-way operators is subject of ongoing research.

Compared to the data domain, the image domain is more robust but not immune from cycle skipping. If the current velocity model is reasonably close to the true model, a cycle skip of the two images is unlikely. The chance of cycle skipping depends not only on the velocity model but also on other factors such as the shot positions and the frequency bandwidth of the signals. By increasing the distance between the shots, we violate the assumption of sharing the same aperture and the potential for cycle skipping grows. Increasing the bandwidth of the signals reduces the wavelength, thus further constraining the maximum distance between adjacent experiments. The shot distance enhances the difference between the apertures of the shots, thus the perturbation computed by image difference can experience cycle skipping and incomplete event cancellation, especially for strong and shallow reflectors. The construction of the image perturbation as the first-order term of a Taylor series expansion removes the sensitivity to this source of cycle skipping. Because the warping vector field captures the information about the shift between the two images, our approach is intrinsically more robust against cycle skipping. The correlation of two signals has lower bandwidth than the input signals: The spectrum of the correlation is equal to the product of the spectra of the input signals. Image warping is based on local correlations; the warping vector field is extracted by picking the maximum of the local correlations between the input images. The shift information has, by construction, lower resolution with respect to direct image difference. This lack of resolution gives our inversion algorithm robustness against cycle-skipping away from the optimal solution, but limits the amount of spatial details we can recover. The quick convergence in the inversion tests and the inability to perfectly flatten the horizontal reflectors in the first example describe the resolution limitations of the method. Moreover, as Larner and Celis (2007) point out, the resolution power of conventional semblance method comes from stacking over many experiments. Our approach considers only two experiments at the time and is derived from differential semblance. Thus, we observe the expected trade off between robustness against cycle skipping and resolution.

Finally, the shot-by-shot approach allows one to potentially bootstrap the MVA procedure without first migrating the whole data set; thus, we can update the velocity model in an iterative fashion with respect to shots. An iterative shot-based inversion has been already proposed in the context of waveform inversion in the data domain (see Chauris and Plessix, 2012); in this paper, we do not iteratively update the model for each consecutive pair of experiments; we instead opt for a more traditional inversion procedure and combine the partial updates from different pairs of shots into a global model update.

Several critical points must be carefully handled. First, because we are using only pairs of experiments, the signal-to-noise ratio can be low and the effectiveness of the algorithm may be hampered by the quality of the data. The sensitivity to the signal-to-noise ratio can be addressed using shot-encoding techniques (Whitmore, 1995; Zhang et al., 2005; Morton and Ober, 1998; Soubaras, 2006; Perrone and Sava, 2012) under the assumption that the different experiments are contaminated by uncorrelated noise. Second, because of cycle skipping between images, our approach can be ineffective if the shots are too far from each other, the velocity model is very inaccurate, or the reflector geometry is complex (e.g., around fault zones or in areas with conflicting dips). The similarity of nearby experiments is an assumption of every differential semblance optimization (DSO-like optimization) scheme; if the particular acquisition geometry or the complex wavepaths create shadow zones or illumination holes, DSO is likely to underperform. Discrepancies in the images are due not only to velocity errors but also to the different set up of the two experiments; if the experiment sampling is coarse (e.g., distant shots or plane waves that have very different ray parameters), we need to guarantee that adjacent experiments share the same aperture. The size of the local window used for computing the image displacements should increase with decreasing depth to capture the apparent larger separation closer to the shot positions. Two shots can be considered adjacent for a deep reflector, and not so for a shallow one, because the aperture of the image changes with depth. A further remark is about the difference between 2D and 3D data: in two dimensions, we can clearly specify an order for the shots along a line, whereas in three dimensions we cannot define a unique ordering because the shots can be placed over a 2D surface, and we do not address the possible strategies to compare shots in a 3D acquisition in this paper. In the shot domain, diving waves create images that do not correspond to reflection events and that do not satisfy the warping relationship assumed in this paper. Analogous considerations apply to multiply scattered wave and converted waves, which are not correctly handled by migration algorithms based on the Born approximation. Apparent reflectors associated with multiples and converted waves do not satisfy the warping relationship we assumed for the definition of the image perturbation, and thus introduce a systematic bias in the inversion scheme. Also, in cases of highly refractive velocity models (Stolk and Symes, 2004), the kinematic artifacts created by the imaging operator can severely affect the inversion, because they do not satisfy the criteria we assume for defining our velocity error measure.

CONCLUSIONS

We introduce a new measure of velocity errors for migration velocity analysis in the shot domain. Our measure is based on an approximation of the difference between the images obtained from adjacent shot-gathers. By using image warping, we can relate the two migrated images, and Taylor-series expansion of one the two images with respect to the warping vector fields can be used to effectively approximate the image difference. The approximation depends on a single migrated image, and thus, by construction, it is more robust against cycle skipping in the image domain.

The image warping approximation of the image difference is constructed by computing the dot product between the gradient of the migrated image and the warping vector field that describes the apparent shift between the two images. For planar reflectors, this quantity can be intuitively related with the angle between the orientation of the reflector and the direction of the displacement vector. When the migration model is accurate, the image gradient is orthogonal to the warping vector field, i.e., the images constructively interfere along the slope of the reflector.

Synthetic tests involving local velocity anomalies and severe focusing and defocusing of the wavefields show the effectiveness of our approach for linearized MVA.

Downloaded 05/08/14 to 138.67.128.110. Redistribution subject to SEG license or copyright; see Terms of Use at http://library.seg.org/

ACKNOWLEDGMENTS

We would like to acknowledge the financial support provided by a research grant from eni E&P. We also thank Jacopo Panizzardi for insightful and helpul comments. The reproducible numeric examples use the Madagascar open-source software package (http://www.ahay.org). We thank Jeff Godwin for integrating the Mines JTK (https://github.com/dhale/jtk) and the Madagascar.

REFERENCES

Aki, K., and P. G. Richards, 2002, Quantitative seismology: University Science Books.

Al-Yahya, K., 1989, Velocity analysis by iterative profile migration: Geophysics, **54**, 718–729, doi: 10.1190/1.1442699.

Biondi, B., and P. Sava, 1999, Wave-equation migration velocity analysis: 69th Annual International Meeting, SEG, Expanded Abstracts, 1723–1726.

Biondi, B., and W. W. Symes, 2004, Angle-domain common-image gathers for migration velocity analysis by wavefield continuation imaging: Geophysics, **69**, 1283–1298, doi: 10.1190/1.1801945.

Bunks, C., F. M. Saleck, S. Zaleski, and G. Chavent, 1995, Multiscale full waveform inversion: Geophysics, **60**, 1457–1473, doi: 10.1190/1.1443880.

Chauris, H., and R.-E. Plessix, 2012, Investigating the differential waveform inversion: 74th Annual Conference and Exhibition, EAGE, Extended Abstracts, Workshops WS06.

Chavent, G., and C. A. Jacewitz, 1995, Determination of background velocities by multiple migration fitting: Geophysics, **60**, 476–490, doi: 10.1190/1.1443785.

Fei, W., and P. Williamson, 2010, On the gradient artifacts in migration velocity analysis based on differential semblance optimization: 80th Annual International Meeting, SEG, Expanded Abstracts, 4071–4076.

Fomel, S., 2002, Applications of plane-wave destruction filters: Geophysics, **67**, 1946–1960, doi: 10.1190/1.1527095.

Hale, D., 2006, Fast local cross-correlations of images: 76th Annual International Meeting, SEG, Expanded Abstracts, 3160–3164.

Hale, D., 2009, A method for estimating apparent displacement vectors from time-lapse seismic images: Geophysics, **74**, no. 5, V99–V107, doi: 10.1190/1.3184015.

Hale, D., B. Cox, and P. J. Hatchell, 2008, Apparent horizontal displacements in time-lapse seismic images: 78th Annual International Meeting, SEG, Expanded Abstracts, 3169–3173.

Larner, K., and V. Celis, 2007, Selective-correlation velocity analysis: Geophysics, **72**, no. 2, U11–U19, doi: 10.1190/1.2435702.

Luo, Y., and G. T. Schuster, 1991, Wave-equation traveltime inversion: Geophysics, **56**, 645–653, doi: 10.1190/1.1443081.

Morton, S. A., and C. C. Ober, 1998, Faster shot-record migration using phase encoding: 68th Annual International Meeting, SEG, Expanded Abstracts, 1131–1134.

Mulder, W. A., and A. P. E. Kroode, 2002, Automatic velocity analysis by differential semblance optimization: Geophysics, **67**, 1184–1191, doi: 10.1190/1.1500380.

Perrone, F., and P. Sava, 2012, Wave-equation migration with dithered plane waves: Geophysical Prospecting, **60**, 444–465, doi: 10.1111/j.1365-2478.2011.01011.x.

Pratt, R. G., 1999, Seismic waveform inversion in the frequency domain, Part 1: Theory and verification in a physical scale model: Geophysics, **64**, 888–901, doi: 10.1190/1.1444597.

Rickett, J., and P. Sava, 2002, Offset and angle-domain common image-point gathers for shot-profile migration: Geophysics, **67**, 883–889, doi: 10.1190/1.1484531.

Sattlegger, J. W., 1975, Migration velocity determination: Part I. Philosophy: Geophysics, **40**, 1–5, doi: 10.1190/1.1440512.

Sava, P., and B. Biondi, 2004, Wave-equation migration velocity analysis. I. Theory: Geophysical Prospecting, **52**, 593–606, doi: 10.1111/j.1365-2478.2004.00447.x.

Sava, P., and S. Fomel, 2006, Time-shift imaging condition in seismic migration: Geophysics, **71**, no. 6, S209–S217, doi: 10.1190/1.2338824.

Sava, P., and I. Vlad, 2008, Numerical implementation of wave-equation migration velocity analysis operators: Geophysics, **73**, no. 5, VE145–VE159, doi: 10.1190/1.2953337.

Shen, P., and W. W. Symes, 2008, Automatic velocity analysis via shot profile migration: Geophysics, **73**, no. 5, VE49–VE59, doi: 10.1190/1.2972021.

Soubaras, R., 2006, Modulated-shot migration: 76th Annual International Meeting, SEG, Expanded Abstracts, 2430–2434.

Soubaras, R., and B. Gratacos, 2007, Velocity model building by semblance maximization of modulated-shot gathers: Geophysics, **72**, no. 5, U67–U73, doi: 10.1190/1.2743612.

Stoffa, P. L., J. T. Fokkema, R. M. de Luna Freire, and W. P. Kessiger, 1990, Split-step Fourier migration: Geophysics, **55**, 410–421, doi: 10.1190/1.1442850.

Stolk, C. C., and W. W. Symes, 2004, Kinematic artifacts in prestack depth migration: Geophysics, **69**, 562–575, doi: 10.1190/1.1707076.

Symes, W. W., 2008, Migration velocity analysis and waveform inversion: Geophysical Prospecting, **56**, 765–790, doi: 10.1111/j.1365-2478.2008.00698.x.

Symes, W. W., and J. J. Carazzone, 1991, Velocity inversion by differential semblance optimization: Geophysics, **56**, 654–663, doi: 10.1190/1.1443082.

Taner, M. T., and F. Koehler, 1969, Velocity spectra — Digital computer derivation and applications of velocity functions: Geophysics, **34**, 859–881, doi: 10.1190/1.1440058.

Tarantola, A., 1984, Inversion of seismic reflection data in the acoustic approximation: Geophysics, **49**, 1259–1266, doi: 10.1190/1.1441754.

van Leeuwen, T., and W. A. Mulder, 2010, A correlation-based misfit criterion for wave-equation traveltime tomography: Geophysical Journal International, **182**, 1383–1394, doi: 10.1111/j.1365-246X.2010.04681.x.

van Vliet, L. J., and P. W. Verbeek, 1995, Estimators for orientation and anisotropy in digitalized images: Proceedings of the First Annual Conference of the Advanced School for Computing and Imaging, ASCI'95, 442–450.

Vasconcelos, I., P. Sava, and H. Douma, 2010, Nonlinear extended images via image-domain interferometry: Geophysics, **75**, no. 6, SA105–SA115, doi: 10.1190/1.3494083.

Vogel, C., 2002, Computational methods for inverse problems: SIAM.

Whitmore, N., 1995, An imaging hierarchy for common-angle plane wave seismograms: Ph.D. thesis, University of Tulsa.

Woodward, M. J., 1992, Wave-equation tomography: Geophysics, **57**, 15–26, doi: 10.1190/1.1443179.

Xie, X. B., and H. Yang, 2008, The finite-frequency sensitivity kernel for migration residual moveout and its applications in migration velocity analysis: Geophysics, **73**, no. 6, S241–S249, doi: 10.1190/1.2993536.

Yang, T., and P. Sava, 2010, Wave-equation migration velocity analysis with extended common-image-point gathers: 80th Annual International Meeting, SEG, Expanded Abstracts, 4369–4374.

Yilmaz, O., 2001, Seismic data processing: SEG.

Zhang, Y., J. Sun, C. Notfors, S. H. Gray, L. Chernis, and J. Young, 2005, Delayed-shot 3D depth migration: Geophysics, **70**, E21–E28, doi: 10.1190/1.2146078.